npj computational materials

www.nature.com/npjcompumats

ARTICLE OPEN

Dynamical phase-field model of coupled electronic and structural processes

Tiannan Yang[1] and Long-Qing Chen[1]✉

Many functional and quantum materials derive their functionality from the responses of both their electronic and lattice subsystems to thermal, electric, and mechanical stimuli or light. Here we propose a dynamical phase-field model for predicting and modeling the dynamics of simultaneous electronic and structural processes and the accompanying mesoscale pattern evolution under static or ultrafast external stimuli. As an illustrative example of application, we study the transient dynamic response of ferroelectric domain walls excited by an ultrafast above-bandgap light pulse. We discover a two-stage relaxational electronic carrier evolution and a structural evolution containing multiple oscillational and relaxational components across picosecond to nanosecond timescales. The phase-field model offers a general theoretical framework which can be applied to a wide range of functional and quantum materials with interactive electronic and lattice orders and phase transitions to understand, predict, and manipulate their ultrafast dynamics and rich mesoscale evolution dynamics of domains, domain walls, and charges.

npj Computational Materials (2022)8:130 ; https://doi.org/10.1038/s41524-022-00820-9

INTRODUCTION

The functionalities of a vast majority of functional materials, including quantum materials, are directly determined from the responses of both of their lattice and electron subsystems to external thermal, mechanical, electric, and magnetic stimuli. For example, in quantum materials, interactions among four fundamental degrees of freedom, i.e., charge, spin, orbit, and lattice are dynamically intertwined, giving rise to complex electronic states and coupled electronic and structural processes[1–3]. At the mesoscale (i.e., from the length of a nanometer to a few microns), emergent orders arise in the form of domains, interfaces, and surfaces etc., exhibiting rich phenomena linking the atomic-scale quantum physics and device-scale applications. Modeling and control of the material at the mesoscale[4] is critical to translating quantum phenomena into functional devices and systems. However, existing mesoscale material models that have been developed for predicting chemical[5–7] and structural[8–10] patterns and processes of classical systems do not apply to systems involving interactive electronic orders. Here we report a computational model for understanding the dynamics of simultaneous structural and electronic processes in functional and quantum materials, discovering their mesoscale fundamental physics, and predicting their functionalities.

As an example, we consider the dynamical interplay between charge and lattice orders to illustrate the application of a generalized phase-field framework[11] to model the excited-state simultaneous evolution dynamics of electronic carriers and structural domains. We consider a specific example involving the excited-state relaxation dynamics of a ferroelectric crystal involving strong charge-lattice coupling. A ferroelectric crystal almost always contains electrically switchable mesoscale domains of spontaneous polarization, separated by uncharged/charged domain walls. Many of the common ferroelectric materials may be considered as wide band-gap semiconductors in which the free electron and hole concentrations, albeit intrinsically low, can be transiently raised by orders of magnitude upon external excitation through diverse types of stimuli such as light or current injections. The excited carriers may possess prolonged lifetimes through polarization-induced band bending[12] and coevolve with lattice responses, giving rise to various transient properties and phenomena vastly different from those of ground states and quasi-static conditions, including enhanced structural responses[13–17], the emergence of metastable phases[18,19], and terahertz radiation[20], etc.

The excited-state dynamics of an inhomogeneous ferroelectric system involves a few essential characters, including both timescale and spatial scale for charge generation, separation, and relaxation, the coupling and decoupling between the carrier and structural domain evolutions, and the role of the type of domain structures, etc. Consider a general case of the evolution of excited carriers in a polar domain structure. Regions with net bound charges like domain walls (as illustrated in Fig. 1) generate local electric potential extrema which serve as traps for charge carriers (i.e., band bending). Upon excitation by any external stimuli, electrons (holes) will migrate and concentrate at positively (negatively) charged regions within a ferroelectric domain structure, leading to charge separation around these regions. This further alters the dipolar electrostatic interaction within the ferroelectric domain structure and may induce a transient response of the polarization as well as a lattice deformation.

The above process involves the evolution of multiple degrees of freedom of the system, which can be described by 4 sets of independent variables, including the ferroelectric polarization $\mathbf{P}(\mathbf{x},t)$, the mechanical displacement $\mathbf{u}(\mathbf{x},t)$, the free electron and hole concentrations $n(\mathbf{x},t)$ and $p(\mathbf{x},t)$, and the electric potential $\Phi(\mathbf{x},t)$. All these variables directly respond to external stimuli while they coevolve interactively with one another, as illustrated in Fig. 2. Existing mesoscale models for ferroelectric domains either neglect the free electrons degree of freedom[21,22] or only consider equilibrium carrier conditions and quasi-static structural kinetics[23–27] for quasi-static timescales, and thus do not apply to the carrier and domain dynamics at nanosecond and shorter timescales. To establish a comprehensive model on the coupled spatiotemporal response of the system, a consistent description of

[1]Department of Materials Science and Engineering, The Pennsylvania State University, University Park, PA 16802, USA. ✉email: lqc3@psu.edu

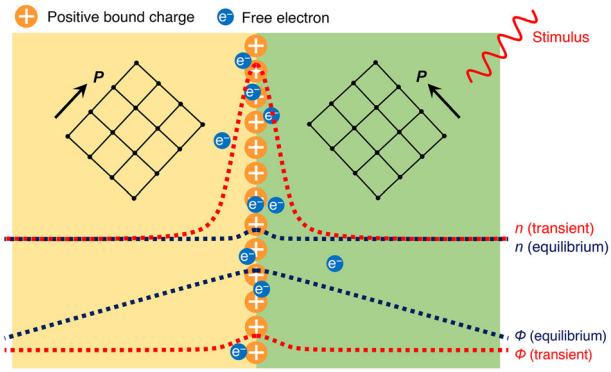

Fig. 1 Schematics of electronic and structural excitation around a charged ferroelectric domain wall. A positively charged ferroelectric domain wall shows a slighted raised electron concentration n and a locally maximized electric potential Φ at equilibrium. Upon excitation by an external stimulus, free electrons will migrate to the domain wall, resulting in an increased local concentration n which will partly compensate the polarization bound charge. This leads to a transient flattening of the electric potential profile Φ around these regions, which may further excite a transient response of the ferroelectric domains.

the time-dependent dynamics of all sets of variables is adopted as follows.

First, the structural dynamics of the system adopts that of a recently developed dynamical phase-field model[28], where the evolution of ferroelectric polarization and mechanical displacement is governed by the polarization dynamics equation and the elastodynamics equation, respectively,

$$\boldsymbol{\mu}\ddot{\mathbf{P}} + \boldsymbol{\gamma}\dot{\mathbf{P}} = -\frac{\delta F}{\delta \mathbf{P}}, \tag{1}$$

$$\rho\ddot{\mathbf{u}} = \nabla \cdot (\boldsymbol{\sigma} + \beta\sigma), \tag{2}$$

where $\boldsymbol{\mu}$ and $\boldsymbol{\gamma}$ are the mass and damping coefficients of polarization dynamics, F is the total free energy of the domain structure[22] with its expression provided in Methods, ρ and β are the material mass density and the stiffness damping coefficient respectively, and $\boldsymbol{\sigma}(\mathbf{x}, t)$ is the stress field.

Second, we incorporate the charge carrier dynamics by temporally and spatially evolving the electron and hole concentrations through transport, generation, and relaxation,

$$\dot{n} = -\nabla \cdot \mathbf{j}_e + S_e + R, \tag{3}$$

$$\dot{p} = -\nabla \cdot \mathbf{j}_h + S_h + R. \tag{4}$$

where $\mathbf{j}_e(\mathbf{x}, t)$ and $\mathbf{j}_h(\mathbf{x}, t)$ are the net fluxes of free electrons and holes, respectively, $S_e(\mathbf{x}, t)$ and $S_h(\mathbf{x}, t)$ are carrier injection rates from external sources, and $R(\mathbf{x}, t)$ is the generation rate of electron-hole pairs. The net carrier fluxes are given by $\mathbf{j}_e = -\frac{\mathbf{M}_e n}{e}\nabla\mu_e$ and $\mathbf{j}_h = -\frac{\mathbf{M}_h p}{e}\nabla\mu_h$, where e is the elementary charge, $\mathbf{M}_e$ and $\mathbf{M}_h$ are the electron and hole mobilities, and $\mu_e(\mathbf{x}, t)$ and $\mu_h(\mathbf{x}, t)$ are their electrochemical potentials. Expressions of μ_e, μ_h, and R are presented in Methods.

Last, the electric potential Φ is given by the electrostatic Poisson equation,

$$\nabla \cdot \left(-\kappa_0 \boldsymbol{\kappa}^b \nabla\Phi + \mathbf{P}\right) = e(p - n). \tag{5}$$

κ_0 and $\boldsymbol{\kappa}^b$ are the vacuum permittivity and background dielectric constant, respectively. Equation (5) incorporates electrostatic interaction among electric polarization and free charge carriers, and thus couples the evolutions of structural domains (Eqs. (1–2)) and carriers (Eqs. (3–4)). This completes the phase-field equation system. A more detailed description of the model is provided in Methods.

RESULTS

To illustrate the application of the model, we consider the excited-state dynamics of typical 90° tetragonal twin domains in a ferroelectric $PbTiO_3$ crystal upon applying an above-bandgap light pulse. Tetragonal domain structures consisting of 90° a_1 and a_2 domains can be classified into three types based on the orientation and the bound charges of the domain wall, including (I) *uncharged head-to-tail domain walls*, (II) pairs of *head-to-head and tail-to-tail domain walls* parallel to each other, and (III) *charged tilted head-to-tail domain walls*, as shown in Fig. 3a. They are defined using the angle between the wall normal and the polarization of the $a_1(a_2)$ domain located at (I) −45°(45°), (II) 45° (135°), and (III) some angle slightly different from −45°(45°) (taking −35°(55°) as an example in the present study), respectively. The bound charge distribution of these types of domain structures in $PbTiO_3$ shows (I) a zero net charge within the uncharged head-to-tail domain walls, (II) high charge density within head-to-head and tail-to-tail domain walls, and (III) intermediate charge density within tilted head-to-tail domain walls. The uncharged domain wall is the most prevalent type of domain walls in $PbTiO_3$, while charged walls also tend to appear within more complicated domain structures or under external constraints[29,30]. To stabilize the highly charged domain structures in (II), a layer of space charges with a fixed area density of -0.02 C m^{-2} and $+0.02$ C m^{-2} are placed along the head-to-head and tail-to-tail walls, respectively, to partially compensate the bound charges. This represents the effect of possible aggregation of charged defects like oxygen vacancies and dislocations at the domain walls.

We apply a 400 nm light pulse with a total fluence of 5 J m^{-2}. The time dependence of the light intensity follows a Gaussian distribution centered at time $t = 1$ ps with an effective duration of 100 fs. We first examine the light-excited strain dynamics by analyzing the response of the average strain $\Delta\varepsilon_{11}$ along the domain wall normal, as presented in Fig. 3b. Of all three domain structures, the head-to-head and tail-to-tail twin domains show the strongest strain responses with a strain increase before $t = 2$ ps, and then remaining relatively steady before $t = 200$ ps except for transient oscillations, till eventually relaxing back to the original equilibrium on a nanosecond timescale. The domains with charged tilted walls show a similar time-dependent response with weaker amplitudes. The twin domains with uncharged walls show the weakest response with only a slight strain oscillation. In all three domain structures, the original strain is recovered within 20 ns.

Carrier dynamics of head-to-head and tail-to-tail domains

To understand the coupled strain and charge carrier responses, we examine the transient carrier and structural evolution within each type of domain structure, starting from the head-to-head and tail-to-tail domains which show the strongest responses. Figure 4 presents the carrier concentration evolution within head-to-head and tail-to-tail domains. The application of the light pulse instantaneously excites electron-hole pairs throughout the domain structure, leading to an almost homogeneous increase in carrier concentrations (around $t = 1$ ps). Then the electrons and holes start migrating in opposite directions due to the electric potential distribution (see Supplementary Fig. 1), with an accumulation (depletion) of electrons (holes) around positively charged head-to-head walls and a depletion (accumulation) around negatively charged tail-to-tail walls, respectively, mostly within the time range of $t < 2$ ps.

Meanwhile, the recombination of excited electrons and holes starts to take place, manifesting in their concentration decreases.

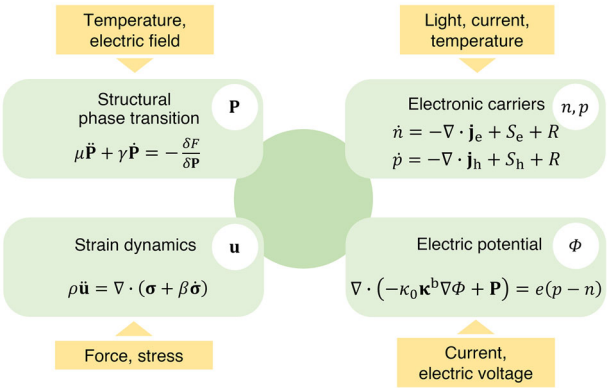

Fig. 2 Diagram of the governing equations of all degrees of freedom of the phase-field model. 4 sets of independent variables are used to describe the electron-lattice system of a ferroelectric semiconductor, including the structural phase order (i.e., ferroelectric polarization) **P**, the mechanical displacement **u**, the free electron and hole concentrations n and p, and the electric potential Φ. The dynamics of these variables can be excited directly by various external stimuli or via the interplay among one-another. A combination of the governing equations of each of the variables yields a complete spatiotemporal description of the coupled dynamics of the charge carriers and structural domains.

The electron-hole recombination process is prominent and almost homogeneous inside a_1 and a_2 ferroelectric domains with a decay time constant of about 4 ps, whereas it is much slower at domain walls leading to a much longer survival time. At head-to-head walls, due to a fast depletion of holes before $t = 10$ ps (see Fig. 4a), the carrier recombination slows down considerably compared to that inside the domains, while electrons are trapped by a local electric potential maximum preventing their migration away from the domain walls. This allows the local electron concentration to remain steady at 10 ps < t < 200 ps, till it further relaxes with a much longer characteristic decay time of about 3 ns. The same applies to tail-to-tail walls, at which electron holes have a considerably prolonged lifetime. As a result, the charge carrier dynamics follows a sequence of excitation, migration, and a two-step relaxation across picosecond to nanosecond timescales.

Structural dynamics of head-to-head and tail-to-tail domains

The transient spatial redistribution of charge carrier further induces structural responses via the electrostatic interaction. Accumulation of electrons and holes at the domain walls within t < 2 ps greatly compensates the bound charges at the walls and flattens the electric potential profile (see Supplementary Fig. 1). Such release of the internal electric field favors an increase of ferroelectric polarization component P_1 parallel to the wall normal and leads to a rotation of the polarization in both domains, as shown in Fig. 5a. This is accompanied by damped oscillations of both P_1 and P_2 which last about 50 ps (see Fig. 5b), showing an intrinsic dielectric response of the polarization. The domain walls also undergo an oscillation of polarization P_2, which has a larger amplitude and a slightly lower frequency compared with the domain interiors, due to the higher local energy and reduced stability of the walls. Such polarization dynamics is coupled to the strain response through piezoelectric coupling and induces a transient tensile strain ε_{11} and subsequent strain oscillations in both the domain interior and domain wall regions, as presented in the bottom panels of Fig. 5a, b. A frequency analysis of the strain oscillation within the first 50 ps (see Supplementary Fig. 2b) reveals two major frequency peaks at 0.45 THz and 0.67 THz, which are mainly attributed to the structural response around the domain walls and that inside the domains, respectively.

After the oscillational responses die out, the polarization and strain evolutions enter a steady stage with a transient change of $\Delta|P_1| = 0.08$ C m^{-2} and $\Delta\varepsilon_{11} = 0.8\%$ inside the domains compared with the original state, as shown in Fig. 5b. Then at the nanosecond timescale, both P_1 and ε_{11} eventually relax back to the original value within t < 20 ns, due to a recovery of the electric potential to the original state (see Supplementary Fig. 1) caused by the decay of carrier concentrations at the domain walls within the same time period. Consequently, the overall structural response of the ferroelectric domains shows a sequence of an initial rapid rise (at 1–2 ps) followed by sub-terahertz damped oscillations (2–50 ps) and a subsequent steady stage (50–200 ps) within the picosecond timescale and a relaxation (200 ps–20 ns) at the nanosecond timescale, closely coupled to the carrier dynamics.

Tilted head-to-tail domains

We next examine the case of tilted head-to-tail domains which shows the second strongest strain response. The strain evolution of the tilted head-to-tail domains (see Fig. 3b) also consists of an initial rise followed by damped oscillations, an intermediate steady stage, and a final relaxation. The corresponding carrier evolution (see Supplementary Fig. 3b) shows a two-step relaxation with an intermediate steady stage (50–200 ps) for the electrons and holes accumulated at the tilted domain walls. Both of the strain and carrier responses are similar to those of the head-to-head and tail-to-tail domains but with notably smaller amplitudes, showing a weaker interaction between carriers and the tilted domains caused by the lower bound charge density of the domain walls. As presented in Fig. 6a, the a_1 and a_2 domains both undergo counterclockwise polarization rotations, leading to a tensile strain change $\Delta\varepsilon_{11}$ in the a_1 domain and a compressive one in the a_2 domain, which partly offset each other and result in a reduced average strain response within the domain structure.

The tilted domains further show a distinctive additional feature of a notable slower oscillational component of strain dynamics with a period on the order of 10 ps. This is attributed to the domain wall motion in addition to the response inside the domains. Due to the different angles of the polarization on the two sides of the domain wall with respect to the wall normal, the tilted head-to-tail domain wall is electrically asymmetric with a higher bound charge density at the a_2 domain-side of the wall than the a_1 domain-side (see Fig. 3a). As a result, light-excited carriers that accumulate around the domain walls (i.e., electrons for positively charged walls and holes for negatively charged walls) tend to tilt towards the a_2 side of the domain walls rather than distribute symmetrically about the walls, inducing a slightly asymmetric electric potential field at the domain wall (see Supplementary Fig. 3a and Supplementary Fig. 5). Such symmetry breaking of the electrostatic condition activates a domain wall motion towards the a_2 domain. As shown in Fig. 6b, the domain wall first oscillates with a maximum amplitude of about 0.5 nm and then stabilizes into an intermediate steady stage until it finally relaxes back to the original position following the nanosecond-timescale carrier relaxation. This generates a strong strain response around the domain wall area, contributing to the observed strain evolution of the twin domains, which shows a superposition of slow and fast oscillational components within the first 50 ps. A frequency analysis of the strain response reveals a 0.06 THz frequency for the domain wall and 0.51 THz and 0.71 THz frequencies for the domains (see Supplementary Fig. 2c). It is further noted that the electronic carriers trapped at the domain walls closely follow the domain wall motions, due to the much shorter response time (<1 ps) of the carrier migration compared with the oscillation period of the domain walls (~17 ps).

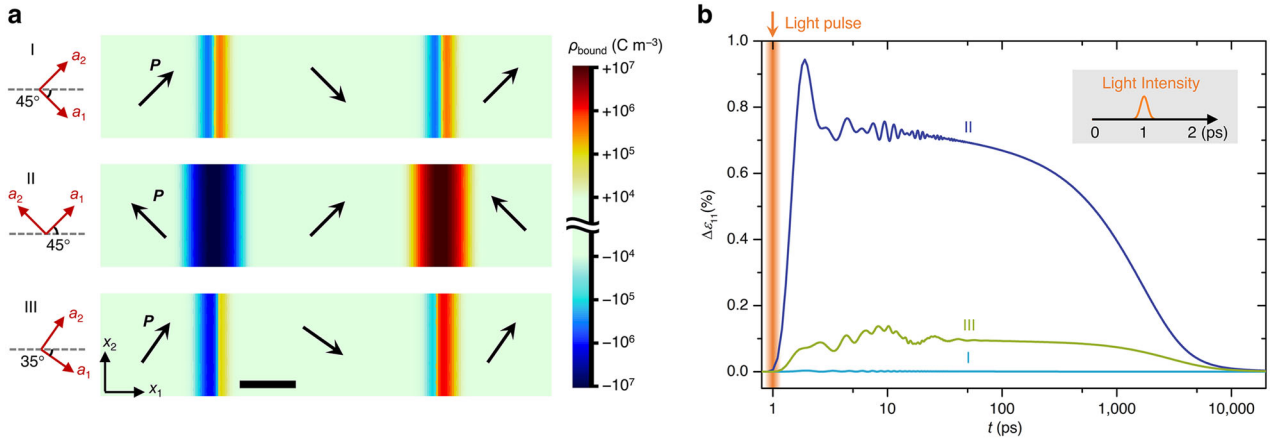

Fig. 3 Types of 90° twin domains and their light-excited strain dynamics. a Three types of 90° a_1-a_2 twin domain structures, including (top panel, I) uncharged head-to-tail domain walls, (middle panel, II) a pair of head-to-head and tail-to-tail domain walls, and (bottom panel, III) charged tilted head-to-tail domain walls, possess different spatial patterns of bound charge densities ρ_{bound}. Polarization directions within each domain (black arrows) as well as crystallographic axes a_1 and a_2 (red arrows) and their angles to the domain wall normal (gray dashed lines) are shown. The scale bar is 5 nm. **b** Upon application of an above-bandgap light pulse, a transient strain response $\Delta\varepsilon_{11}$ is induced in all three structures within picosecond-to-nanosecond timescales. The head-to-head and tail-to-tail twin domains (II) show the strongest strain response, while the uncharged twin domains (I) show the weakest response. The inset shows the shape of the applied light pulse centered at $t = 1$ ps.

Head-to-to-tail domains

For the uncharged head-to-tail domains, the overall strain dynamics shows the weakest strain response with only a small oscillation at the nanosecond timescale and no transient steady-state stage. The light-induced evolution of carrier concentration, polarization, strain, and electric potential is provided in Supplementary Figs. 6–8. The uncharged domain walls have very small amounts of charge with opposite signs on two sides of the wall and a zero net charge (see Fig. 3a), which exhibit an almost flat equilibrium electric potential. Thus, these walls interact very weakly with free carriers, resulting in a single-component fast relaxation of the carrier concentration upon light excitation. The polarization and strain dynamics both show a weak oscillational response at a picosecond timescale, indicating a slight loosening of the domain walls.

DISCUSSION

The proposed phase-field model integrates the dynamical phase-field equations for both electronic and lattice subsystems at the mesoscale. It offers a theoretical framework for understanding and predicting the coupled electron and structural dynamics of excited states in materials that possess interactive charge, polarization, and lattice orders. It also lays the foundation for further application of mesoscale models to a wide variety of functional and quantum materials to understand and control their mesoscale quantum phenomena and translating them into next-generation functional devices. Future model development may advance towards specific materials systems like topological insulators and high-temperature superconductors, through further incorporating the evolution dynamics of additional degrees of freedom including electronic phase orders and spin orders etc., as well as the cross-coupling mechanisms among them.

In the present example of the light excitation of $PbTiO_3$ ferroelectric domains, the proposed phase-field model reveals the following information. First, it provides the timescales of charge separation within the ferroelectric domain structure and the dynamics of a two-component charge relaxation with different timescales for free electronic carriers and carriers trapped by the domain walls. Second, it predicts the response of structural domains that coevolve with carriers, containing several picosecond oscillational components and a nanosecond relaxational component, indicating rich dynamics involving domains, domain walls, and charges. Similar light-induced transient strain with notable components at both picosecond and nanosecond timescales has also been experimentally captured in $PbTiO_3$ and $BiFeO_3$ films[14,31], in agreement with our simulation. Also note that in the present example, although the coupled electronic processes strongly affect the excited-state transient structural processes, its influence on the equilibrium-state domain structure is negligible due to the very low equilibrium concentration of electronic charge carriers of the wide-bandgap semiconductor. The equilibrium domain structure of twin domains both before and after the excitation converges to previous theoretical predictions that did not account for electronic processes[32,33]. However, for doped systems, systems containing charged defects, or metallic systems, the equilibrium electronic carrier concentration may become significant in determining the equilibrium-state domain structure. Last, it captures the role of different types of domain walls in determining the electron-lattice interactions. The current phase-field model can also be applied to study the mesoscale evolution of other coupled electronic and structural processes of theoretical interests in various ferroelectric materials, including nucleation of domains and transition of topological phases[34–36] assisted by excited carriers. The theoretical insights on the carrier-related ferroelectric dynamics provide guidance for controlling the generation, relaxation, and transport of charge carriers, which is essential to the development of a number of emergent ferroelectric functionalities, such as domain wall conduction[37–40] and bulk photovoltaic effect[41,42].

METHODS

Basic variables and their governing equations

The electron-lattice system is described using 4 sets of independent variables that are spatially inhomogeneous over position $\mathbf{x}$ and evolving with time t, including the ferroelectric polarization $\mathbf{P}(\mathbf{x}, t)$, the mechanical displacement $\mathbf{u}(\mathbf{x}, t)$, the free electron and hole concentrations $n(\mathbf{x}, t)$ and $p(\mathbf{x}, t)$, and the electric potential $\Phi(\mathbf{x}, t)$. A set of governing equations are solved for the time-dependent evolution of these variables:

The evolution of polarization field $\mathbf{P}$ follows the polarization dynamics equation[28],

$$\boldsymbol{\mu}\ddot{\mathbf{P}} + \boldsymbol{\gamma}\dot{\mathbf{P}} = -\frac{\delta F}{\delta \mathbf{P}}, \tag{6}$$

$\boldsymbol{\mu}$ and $\boldsymbol{\gamma}$ are the mass and damping coefficients of the polarization. F is the total free energy of the system with expression provided in the next section.

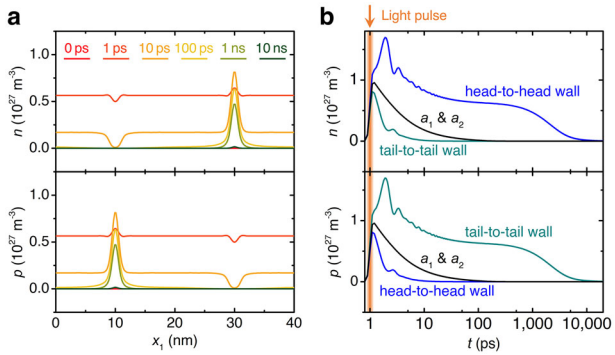

Fig. 4 Charge carrier dynamics in 90° domains with head-to-head and tail-to-tail domain walls. a Spatial distribution at selected times. **b** Their temporal evolution inside a_1 and a_2 domains and at the center of domain walls.

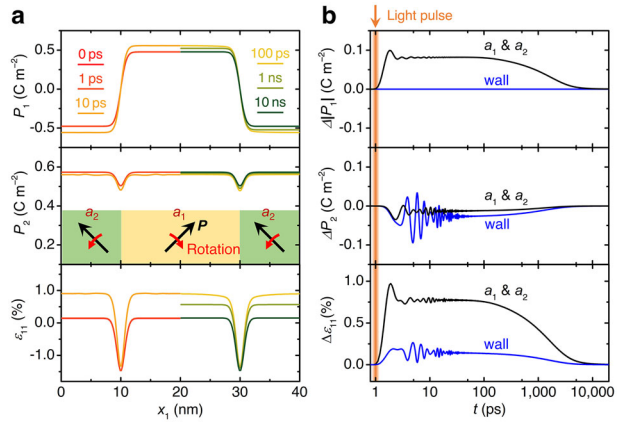

Fig. 5 Structural dynamics in 90° domains with head-to-head and tail-to-tail domain walls. a Spatial distribution of initial and excited-state polarization P_1, P_2, and strain ε_{11} at selected times. All 3 fields are symmetric about $x_1 = 20$ nm. For clarity, we only show the $x_1 <$ 20 nm half of the data at $t \leq 10$ ps and $x_1 > 20$ nm half of the data at $t > 10$ ps. The middle panel contains a schematic showing polarization rotation of each domain. The average lattice parameter within the whole sample before the light excitation is used as a reference for calculating ε_{11}, i.e., the average original ε_{11} is set as zero. **b** Temporal evolution of the changes $\Delta|P_1|$, ΔP_2, and $\Delta\varepsilon_{11}$ inside a_1 and a_2 domains and at the center of domain walls, with respect to the initial state.

The mechanical displacement $\mathbf{u}$ is governed by the elastodynamics equation[28],

$$\rho\ddot{\mathbf{u}} = \nabla \cdot (\boldsymbol{\sigma} + \beta\dot{\boldsymbol{\sigma}}), \tag{7}$$

ρ and β are the material mass density and the stiffness damping coefficient, respectively. $\boldsymbol{\sigma}(\mathbf{x}, t)$ is the stress field, dependent on the structural variables through the Hooke's law $\sigma_{ij} = c_{ijkl}\left(\varepsilon_{kl} - \varepsilon^0_{kl}\right)$, where $\mathbf{c}$ is the elastic stiffness tensor, $\boldsymbol{\varepsilon}(\mathbf{x}, t)$ is the strain field given by $\boldsymbol{\varepsilon} = [\nabla\mathbf{u} + (\nabla\mathbf{u})^T]/2$, and $\boldsymbol{\varepsilon}^0(\mathbf{x}, t)$ is the eigenstrain field given by $\varepsilon^0_{ij} = Q_{ijkl}P_kP_l$, with $\mathbf{Q}$ being the electrostrictive coefficient. An Einstein summation convention of automatic summation over repeated indices $i, j, k, l = 1, 2, 3$ is employed herein.

The evolution of the electron and hole concentrations follows the electron transport equations,

$$\dot{n} = -\nabla \cdot \mathbf{j}_e + S_e + R, \tag{8}$$

$$\dot{p} = -\nabla \cdot \mathbf{j}_h + S_h + R, \tag{9}$$

$\mathbf{j}_e(\mathbf{x}, t)$ and $\mathbf{j}_h(\mathbf{x}, t)$ are the net fluxes of free electrons and holes, respectively, given by $\mathbf{j}_e = -\frac{\mathbf{M}_e n}{e}\nabla\mu_e$ and $\mathbf{j}_h = -\frac{\mathbf{M}_h p}{e}\nabla\mu_h$, where e is the elementary charge. Here $\mathbf{M}_e$ and $\mathbf{M}_h$ are the electron and hole mobilities, and $\mu_e(\mathbf{x}, t)$ and $\mu_h(\mathbf{x}, t)$ are their electrochemical potentials which are formulated as functions of n and p with given information on the electronic band structure. $S_e(\mathbf{x}, t)$ and $S_h(\mathbf{x}, t)$ are carrier injection rates from external sources, taken as zero in the present paper. $R(\mathbf{x}, t)$ is the generation rate of electron-hole pairs which may include contributions from intrinsic electron-hole creation/recombination and light-induced excitation. Note that in a polar microstructure with strong internal electrostatic fields, an electron-hole pair will separate almost instantly upon excitation, so we herein neglect the exciton (i.e., excited bound electron-hole pair) concentration which has been used as an additional independent variable for the excited electronic system in some theoretical models[43,44].

The electric potential Φ is governed by the electrostatic Poisson equation,

$$\nabla \cdot \left(-\kappa_0\boldsymbol{\kappa}^b\nabla\Phi + \mathbf{P}\right) = e(p - n). \tag{10}$$

κ_0 and $\boldsymbol{\kappa}^b$ are the vacuum permittivity and background dielectric constant, respectively.

A combination of Eqs. (6–10) provides a complete description of the dynamics of the charge carriers and structural domains. By numerically solving Eqs. (6–10), we obtain the spatiotemporal response of the coupled electron-lattice system under given conditions and external stimuli. Material constants of $PbTiO_3$ are provided in Supplementary Table 1. Computer simulations are performed using the Extreme Science and Engineering Discovery Environment (XSEDE)[45].

Free energy of the ferroelectric domains

The thermodynamics of the ferroelectric domains follows those of existing phase-field models[22]. The free energy F is formulated as the sum of the Landau free energy, the gradient energy, the electrostatic energy, and the elastic energy, i.e.,

$$F = F_{\text{Landau}} + F_{\text{gradient}} + F_{\text{electrostatic}} + F_{\text{elastic}}. \tag{11}$$

The energy contributions are given by

$$F_{\text{Landau}} = \int \left(a_iP_i^2 + a_{ij}P_i^2P_j^2 + a_{ijk}P_i^2P_j^2P_k^2\right)dx^3, \tag{12}$$

$$F_{\text{gradient}} = \int g_{ijkl}\frac{\partial P_i}{\partial x_j}\frac{\partial P_k}{\partial x_l}dx^3. \tag{13}$$

$$F_{\text{electrostatic}} = \int \left(-\frac{1}{2}\kappa_0\kappa^b_{ij}E_iE_j - E_iP_i\right)dx^3, \tag{14}$$

$$F_{\text{elastic}} = \int \frac{1}{2}c_{ijkl}\left(\varepsilon_{ij} - \varepsilon^0_{ij}\right)\left(\varepsilon_{kl} - \varepsilon^0_{kl}\right)dx^3, \tag{15}$$

a_i, a_{ij}, and a_{ijk} are the Landau coefficients, $\mathbf{g}$ is the gradient energy coefficient, and $\mathbf{E}(\mathbf{x}, t)$ is the electric field given by $\mathbf{E} = -\nabla\Phi$. Equation (14) indicates a coupling between the structural evolution and the carrier evolution through electrostatic interaction.

Electrochemical potentials of charge carriers

We formulate the electrochemical potentials μ_e and μ_h as functions of variables n, p, and Φ. For simplicity, we take a parabolic assumption of the density of states $D(\xi)$ in both the conduction band and the valence band, following

$$D = K_{DC}(\xi - E_C + e\Phi)^{1/2}, \tag{16}$$

$$D = K_{DV}(-\xi + E_V - e\Phi)^{1/2}, \tag{17}$$

where E_C and E_V are the energy levels at the bottom of the conduction band and the top of the valence band, respectively. K_{BC} and K_{DV} are material constants related to effective electron mass and effective hole mass through $K_{DC} = \frac{\sqrt{2}m_e^{*3/2}}{\pi^2\hbar^3}$ and $K_{DV} = \frac{\sqrt{2}m_h^{*3/2}}{\pi^2\hbar^3}$, where $\hbar$ is the reduced Planck constant. The values of K_{DV} and K_{DC} for $PbTiO_3$ are fitted using the density of states data in ref. [46]. Following Fermi statistics, the electrochemical potentials of electrons in the conduction band and holes in the valence band are related to local electron and hole

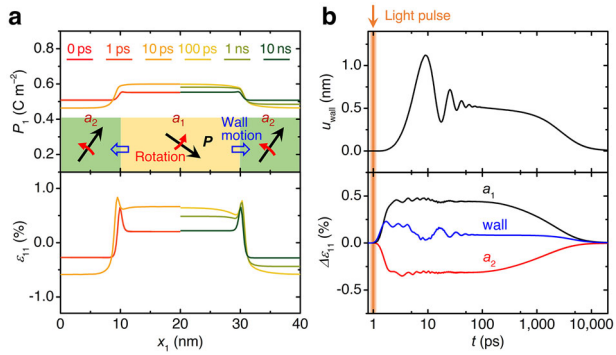

Fig. 6 Structural dynamics in 90° domains with tilted domain walls. a Spatial distribution of initial and excited-state polarization P_1 and strain ε_{11} at selected times. Both fields are symmetric about $x_1 = 20$ nm. For clarity, we only show the $x_1 < 20$ nm half of the data at $t \leq 10$ ps and $x_1 > 20$ nm half of the data at $t > 10$ ps. The top panel contains a schematic showing polarization rotation of each domain and motion of domain walls. **b** Temporal evolution of the domain wall displacement u_{wall} as well as light-induced strain change $\Delta\varepsilon_{11}$ inside a_1 and a_2 domains and at the center of domain walls. Corresponding polarization evolution is shown in Supplementary Fig. 4.

concentrations n and p as well as electric potential Φ through

$$\mu_{\mathrm{e}} = E_{\mathrm{C}} - e\Phi + k_{\mathrm{B}}TF_{1/2}^{-1}\left(\frac{2n}{\sqrt{\pi}k_{\mathrm{B}}^{3/2}T^{3/2}K_{\mathrm{DC}}}\right), \tag{18}$$

$$\mu_{\mathrm{h}} = -E_{\mathrm{V}} + e\Phi + k_{\mathrm{B}}TF_{1/2}^{-1}\left(\frac{2p}{\sqrt{\pi}k_{\mathrm{B}}^{3/2}T^{3/2}K_{\mathrm{DV}}}\right). \tag{19}$$

Here k_{B} is the Boltzmann constant, T is the temperature, and $F_{1/2}^{-1}(x)$ is the inverse function of the Fermi integral with an order of 1/2. Using the center of the band gap as a reference, for chemically homogeneous systems, it follows $E_{\mathrm{C}} = E_{\mathrm{g}}/2$ and $E_{\mathrm{V}} = -E_{\mathrm{g}}/2$, with E_{g} being the band gap width. Here we neglect the effect of band bending due to chemical inhomogeneities, including impurities and vacancies as has been reported by first-principles studies[47,48]. For chemically inhomogeneous systems, E_{C} and E_{V} in Eqs. (16–19) may take spatially inhomogeneous values that are determined by the local chemistry.

Generation rate of charge carriers

The generation rate R of electron-hole pairs including contributions from intrinsic electron-hole creation and above-bandgap light excitation is given by[49]

$$R = K_{\mathrm{eh}}\left(n_{\mathrm{eq}}p_{\mathrm{eq}} - np\right) + R_{\mathrm{light}}, \tag{20}$$

where K_{eh} is a material constant related to the electron lifetime, and n_{eq} and p_{eq} are the equilibrium electron and hole concentrations, respectively, given by Eqs. (18–19) under the condition $\mu_{\mathrm{e,eq}} + \mu_{\mathrm{h,eq}} = 0$. $R_{\mathrm{light}}(\mathbf{x}, t)$ is the light-induced excitation rate determined by the light input and the band structure. Under an assumption of a two-parabolic-band model, R_{light} is given by the Fermi's golden rule, written as[50]

$$R_{\mathrm{light}} = \frac{\sqrt{2\left(\hbar\omega - E_{\mathrm{g}}\right)}\pi K_{\mathrm{DV}}e^2E_{\mathrm{g}}I}{2\kappa_0 c m_{\mathrm{e}}\omega^2\hbar}\left(1 + \frac{m_{\mathrm{e}}}{m_{\mathrm{h}}^*}\right)g_{\mathrm{F}}\left(\mu_{\mathrm{h}} - \frac{\hbar\omega}{2}\right)g_{\mathrm{F}}\left(\mu_{\mathrm{e}} - \frac{\hbar\omega}{2}\right), \tag{21}$$

with $K_{\mathrm{DC}} = K_{\mathrm{DV}}$ taken for simplicity. Here ω and I are the angular frequency and intensity of the light, respectively. $g_{\mathrm{F}}(\mu)$ is the Fermi distribution function, expressed as

$$g_{\mathrm{F}}(\mu) = \frac{1}{\exp\left(\frac{\mu}{k_{\mathrm{B}}T}\right) + 1}. \tag{22}$$

DATA AVAILABILITY

The main data supporting the findings of this study are available within the article and its Supplementary information. Additional data are available from the corresponding author upon reasonable request.

Received: 15 March 2022; Accepted: 29 May 2022;
Published online: 22 June 2022

REFERENCES

1. Keimer, B. & Moore, J. The physics of quantum materials. *Nat. Phys.* **13**, 1045–1055 (2017).
2. Tokura, Y., Kawasaki, M. & Nagaosa, N. Emergent functions of quantum materials. *Nat. Phys.* **13**, 1056–1068 (2017).
3. Cava, R., de Leon, N. & Xie, W. Introduction: Quantum Materials. *Chem. Rev.* **121**, 2777–2779 (2021).
4. Yip, S. & Short, M. P. Multiscale materials modelling at the mesoscale. *Nat. Mater.* **12**, 774–777 (2013).
5. Rickman, J. M., Tong, W. S. & Barmak, K. Impact of heterogeneous boundary nucleation on transformation kinetics and microstructure. *Acta Mater.* **45**, 1153–1166 (1997).
6. Boettinger, W. J., Warren, J. A., Beckermann, C. & Karma, A. Phase-Field Simulation of Solidification. *Annu. Rev. Mater. Res.* **32**, 163–194 (2002).
7. Swift, M. W., Swift, J. W. & Qi, Y. Modeling the electrical double layer at solid-state electrochemical interfaces. *Nat. Comput. Sci.* **1**, 212–220 (2021).
8. Artemev, A., Jin, Y. & Khachaturyan, A. Three-dimensional phase field model of proper martensitic transformation. *Acta Mater.* **49**, 1165–1177 (2001).
9. Jin, Y. M. Domain microstructure evolution in magnetic shape memory alloys: phase-field model and simulation. *Acta Mater.* **57**, 2488–2495 (2009).
10. Chen, K., Srolovitz, D. J. & Han, J. Grain-boundary topological phase transitions. *Proc. Natl Acad. Sci. USA* **117**, 33077–33083 (2020).
11. Provatas, N. & Elder, K. *Phase-field methods in materials science and engineering* (John Wiley & Sons, 2011).
12. Morris, M. R., Pendlebury, S. R., Hong, J., Dunn, S. & Durrant, J. R. Effect of internal electric fields on charge carrier dynamics in a ferroelectric material for solar energy conversion. *Adv. Mater.* **28**, 7123–7128 (2016).
13. Korff Schmising, C. V. et al. Coupled Ultrafast Lattice and Polarization Dynamics in Ferroelectric Nanolayers. *Phys. Rev. Lett.* **98**, 257601 (2007).
14. Wen, H. et al. Electronic Origin of Ultrafast Photoinduced Strain in $BiFeO_3$. *Phys. Rev. Lett.* **110**, 037601 (2013).
15. Lejman, M. et al. Giant ultrafast photo-induced shear strain in ferroelectric $BiFeO_3$. *Nat. Commun.* **5**, 4301 (2014).
16. Matzen, S. et al. Tuning Ultrafast Photoinduced Strain in Ferroelectric-Based Devices. *Adv. Electron. Mater.* **5**, 1800709 (2019).
17. Lee, H. J. et al. Structural evidence for ultrafast polarization rotation in ferroelectric/dielectric superlattice nanodomains. *Phys. Rev. X* **11**, 031031 (2021).
18. Stoica, V. A. et al. Optical creation of a supercrystal with three-dimensional nanoscale periodicity. *Nat. Mater.* **18**, 377–383 (2019).
19. Ahn, Y. et al. Nanosecond optically induced phase transformation in compressively strained $BaTiO_3$ on $LaAlO_3$. *Phys. Rev. Lett.* **123**, 045703 (2019).
20. Takahashi, K., Kida, N. & Tonouchi, M. Terahertz Radiation by an Ultrafast Spontaneous Polarization Modulation of Multiferroic $BiFeO_3$ Thin Films. *Phys. Rev. Lett.* **96**, 117402 (2006).
21. Nambu, S. & Sagala, D. A. Domain formation and elastic long-range interaction in ferroelectric perovskites. *Phys. Rev. B* **50**, 5838 (1994).
22. Chen, L.-Q. Phase-Field Method of Phase Transitions/Domain Structures in Ferroelectric Thin Films: A Review. *J. Am. Ceram. Soc.* **91**, 1835–1844 (2008).
23. Sluka, T., Tagantsev, A. K., Damjanovic, D., Gureev, M. & Setter, N. Enhanced electromechanical response of ferroelectrics due to charged domain walls. *Nat. Commun.* **3**, 748 (2012).
24. Eliseev, E. A. et al. Structural phase transitions and electronic phenomena at 180-degree domain walls in rhombohedral BaTiO 3. *Phys. Rev. B* **87**, 054111 (2013).
25. Zuo, Y., Genenko, Y. A. & Xu, B.-X. Charge compensation of head-to-head and tail-to-tail domain walls in barium titanate and its influence on conductivity. *J. Appl. Phys.* **116**, 044109 (2014).
26. Li, L. et al. Giant Resistive Switching via Control of Ferroelectric Charged Domain Walls. *Adv. Mater.* **28**, 6574–6580 (2016).
27. Misirlioglu, I. & Alpay, S. Compositionally graded ferroelectrics as wide band gap semiconductors: Electrical domain structures and the origin of low dielectric loss. *Acta Mater.* **122**, 266–276 (2017).

28. Yang, T., Wang, B., Hu, J.-M. & Chen, L.-Q. Domain Dynamics under Ultrafast Electric-Field Pulses. *Phys. Rev. Lett.* **124**, 107601 (2020).
29. Han, M.-G. et al. Coupling of bias-induced crystallographic shear planes with charged domain walls in ferroelectric oxide thin films. *Phys. Rev. B* **94**, 100101 (R) (2016).
30. Wei, X.-K. et al. Controlled Charging of Ferroelastic Domain Walls in Oxide Ferroelectrics. *ACS Appl. Mater. Interfaces* **9**, 6539–6546 (2017).
31. Daranciang, D. et al. Ultrafast Photovoltaic Response in Ferroelectric Nanolayers. *Phys. Rev. Lett.* **108**, 087601 (2012).
32. Sridhar, N., Rickman, J. M. & Srolovitz, D. J. Twinning in thin films—I. Elastic analysis. *Acta Mater.* **44**, 4085–4096 (1996).
33. Sridhar, N., Rickman, J. M. & Srolovitz, D. J. Twinning in thin films—II. Equilibrium microstructures. *Acta Mater.* **44**, 4097–4113 (1996).
34. Yadav, A. K. et al. Observation of polar vortices in oxide superlattices. *Nature* **530**, 198–201 (2016).
35. Das, S. et al. Observation of room-temperature polar skyrmions. *Nature* **568**, 368–372 (2019).
36. Yang, T., Dai, C., Li, Q., Wen, H. & Chen, L.-Q. Condensation of collective polar vortex modes. *Phys. Rev. B* **103**, L220303 (2021).
37. Seidel, J. et al. Conduction at domain walls in oxide multiferroics. *Nat. Mater.* **8**, 229–234 (2009).
38. Catalan, G., Seidel, J., Ramesh, R. & Scott, J. F. Domain wall nanoelectronics. *Rev. Mod. Phys.* **84**, 119 (2012).
39. Morozovska, A. N., Vasudevan, R. K., Maksymovych, P., Kalinin, S. V. & Eliseev, E. A. Anisotropic conductivity of uncharged domain walls in $BiFeO_3$. *Phys. Rev. B* **86**, 085315 (2012).
40. Vasudevan, R. K. et al. Domain wall conduction and polarization-mediated transport in ferroelectrics. *Adv. Funct. Mater.* **23**, 2592–2616 (2013).
41. Zenkevich, A. et al. Giant bulk photovoltaic effect in thin ferroelectric $BaTiO_3$ films. *Phys. Rev. B* **90**, 161409(R) (2014).
42. Tan, L. Z. et al. Shift current bulk photovoltaic effect in polar materials—hybrid and oxide perovskites and beyond. *npj Comput. Mater.* **2**, 1–12 (2016).
43. Kodali, H. K. & Ganapathysubramanian, B. Computer simulation of heterogeneous polymer photovoltaic devices. *Modell. Simul. Mater. Sci. Eng.* **20**, 035015 (2012).
44. Lee, X. Y. et al. Fast inverse design of microstructures via generative invariance networks. *Nat. Comput. Sci.* **1**, 229–238 (2021).
45. Towns, J. et al. XSEDE: accelerating scientific discovery. *Comput. Sci. Eng.* **16**, 62–74 (2014).
46. de Lazaro, S., Longo, E., Sambrano, J. R. & Beltrán, A. Structural and electronic properties of $PbTiO_3$ slabs: a DFT periodic study. *Surf. Sci.* **552**, 149–159 (2004).
47. Qi, T., Grinberg, I. & Rappe, A. M. Band-gap engineering via local environment in complex oxides. *Phys. Rev. B* **83**, 224108 (2011).
48. Qi, T. et al. First-principles study of band gap engineering via oxygen vacancy doping in perovskite $ABB'O_3$ solid solutions. *Phys. Rev. B* **84**, 245206 (2011).
49. Shi, Y. & Chen, L.-Q. Current-Driven Insulator-To-Metal Transition in Strongly Correlated VO2. *Phys. Rev. Appl* **11**, 014059 (2019).
50. Shi, Y. & Chen, L.-Q. Spinodal electronic phase separation during insulator-metal transitions. *Phys. Rev. B* **102**, 195101 (2020).

ACKNOWLEDGEMENTS

The work is supported as part of the Computational Materials Sciences Program funded by the U.S. Department of Energy, Office of Science, Basic Energy Sciences, under Award No. DE-SC0020145. The computer simulations in this work are performed using the Extreme Science and Engineering Discovery Environment (XSEDE), which is supported by National Science Foundation grant number ACI-1548562; specifically, it uses the Bridges-2 system supported by NSF award number ACI-1928147, at the Pittsburgh Supercomputing Center (PSC).

AUTHOR CONTRIBUTIONS

L.-Q.C. directed and supervised the project. T.Y. performed the simulation and analysis. Both authors wrote the manuscript together.

COMPETING INTERESTS

The authors declare no competing interests.

ADDITIONAL INFORMATION

Supplementary information The online version contains supplementary material available at https://doi.org/10.1038/s41524-022-00820-9.

Correspondence and requests for materials should be addressed to Long-Qing Chen.

Reprints and permission information is available at http://www.nature.com/reprints

Publisher's note Springer Nature remains neutral with regard to jurisdictional claims in published maps and institutional affiliations.

Open Access This article is licensed under a Creative Commons Attribution 4.0 International License, which permits use, sharing, adaptation, distribution and reproduction in any medium or format, as long as you give appropriate credit to the original author(s) and the source, provide a link to the Creative Commons license, and indicate if changes were made. The images or other third party material in this article are included in the article's Creative Commons license, unless indicated otherwise in a credit line to the material. If material is not included in the article's Creative Commons license and your intended use is not permitted by statutory regulation or exceeds the permitted use, you will need to obtain permission directly from the copyright holder. To view a copy of this license, visit http://creativecommons.org/licenses/by/4.0/.

© The Author(s) 2022